Journal of
Synchrotron
Radiation

ISSN 0909-0495

Received 13 May 2010
Accepted 4 August 2010

Ratio-contrast imaging of dual-energy absorption for element mapping with a scanning transmission X-ray microscope

X. Z. Zhang,[a] Z. J. Xu,[a] R. Z. Tai,[a]* X. J. Zhen,[a] Y. Wang,[a] Z. Guo,[a] R. Yan,[a] R. Chang,[a] B. Wang,[b] M. Li,[b] J. Zhao[c] and F. Gao[c]

[a]Shanghai Institute of Applied Physics, Chinese Academy of Sciences, Shanghai 201204, People's Republic of China, [b]CAS Key Laboratory for Biomedical Effects of Nanomaterials and Nanosafety and Key Laboratory of Nuclear Analytical Techniques, Institute of High Energy Physics, Chinese Academy of Sciences, PO Box 918, Beijing 100049, People's Republic of China, and [c]Institute of Chemistry, Chinese Academy of Sciences, Beijing 100190, People's Republic of China. E-mail: tairenzhong@sinap.ac.cn

The detection of chemical mapping with a spatial resolution of 30 nm has been achieved with a scanning transmission X-ray microscope at the Shanghai Synchrotron Radiation Facility. For each specimen, two absorption images were scanned separately with energies E_1 and E_2: E_1 was focused on the absorption edge of the chosen element and E_2 was focused below the edge. A K-edge division method is proposed and applied to obtain the element mapping. Compared with the frequently used K-edge subtraction method, this ratio-contrast method is shown to be more accurate and sensitive in identifying the elements of interest, where the definition of the contrast threshold is simple and clear in physics. Several examples are presented to illustrate the effectiveness of the method.

Keywords: X-ray absorption edge; X-ray microscopy; element microanalysis.

1. Introduction

In both traditional X-ray absorption-contrast imaging and X-ray phase-contrast imaging that has been developed in recent years, the imaging contrast is derived from the interaction of X-rays with the sample. As one of the most commonly used X-ray microscopy analysis methods, the dual-energy contrast imaging method makes use of the abrupt change in X-ray attenuation of a specimen when the incident photon energy changes from just below the absorption edge of a certain element in the sample to just above it. In this method, two absorption-contrast images need to be scanned separately at energies E_1 and E_2, where E_1 is focused below and E_2 above the absorption edge of the element. Because the change in photon energies is only a few percent or less, the absorption of X-rays by all the other elements in the specimen is negligible, and consequently any observed difference in the transmitted X-ray flux between the two images obtained at the two energies can be attributed to the presence of the element being studied (Rarback *et al.*, 1987). With this method the measurement of elemental spatial distributions has been achieved using various light sources (Houk *et al.*, 1979; Sarnelli *et al.*, 2004, 2006; Umetani *et al.*, 1996) and has been widely applied to many science fields, especially in the medical area (Lewis, 1997; Krug *et al.*, 2006; Bewer *et al.*, 2008; Takeda *et al.*, 1998). Among these light sources, synchrotron radiation offers several advantages for absorption-contrast imaging, such as high intensity, high brilliance, natural collimation of the radiation, and energy consecutive tunability of the emitted X-rays, which makes it possible to select a narrow wavelength band with a monochromator (Suortti & Thomlinson, 2003). These advantages are easily exploited by the scanning transmission X-ray microscopy (STXM) technique because of its high detection accuracy of X-rays transmitted through the specimen. Synchrotron-radiation-based STXM is especially suited for studying the distribution of organic K-edge and metal L-edge speciation at a spatial scale of tens of nanometres (Lerotic *et al.*, 2004). With the STXM technique, the Shanghai Synchrotron Radiation Facility (SSRF) achieved a spatial resolution of about 30 nm, which made it possible to map the fine-element distribution and the high-performance monochromator in the beamline.

A frequently used method to trace elements by X-ray imaging is K-edge subtraction (KES) (Jacobson, 1953; Kruger *et al.*, 1977; Fukagawa *et al.*, 1989; Elleaume *et al.*, 2000), which involves subtracting the results of the corresponding pixels' signals in the two images. In this method the threshold of the resulting contrast image that is used to determine whether a pixel contains the specified element cannot be determined directly from theory and relies on the different devices and

experiment results. In fact, there is no standard way to determine the threshold in the conventional subtraction method, and it is usually set arbitrarily; thus, the corresponding result is quantitatively uncertain. In this paper the *K*-edge ratio was used to study the element distribution instead of *K*-edge subtraction. The results show that the contrast threshold can be defined clearly in physics and calculated simply in theory. Moreover, the elemental distributions can be acquired more quantitatively and precisely than those using the KES method. Using this method, for example, the distribution map of phosphorous can be obtained by digital division of two absorption-contrast images at photon energies of 137 eV (at the P 2*p* peak) and 133 eV (pre-peak). Similarly, the K, N, S, Na and Ca maps could be obtained by the digital ratios of 297 and 296 eV, 397 and 394 eV, 178 and 176 eV, 1049 and 1033 eV, and 346 and 345 eV images, respectively (Frazer *et al.*, 2003).

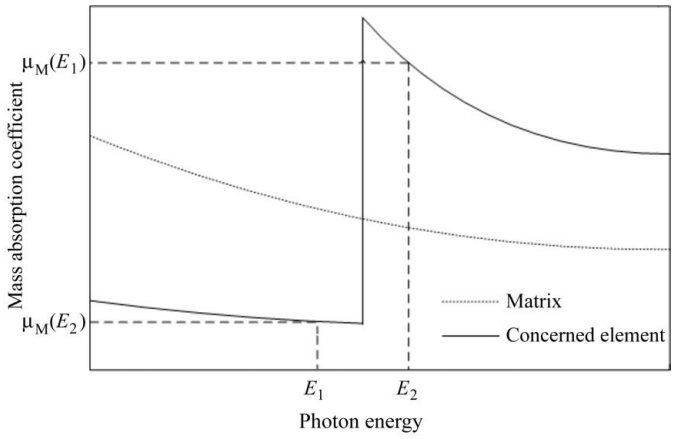

Figure 1
The two energies, E_1 and E_2, chosen to be below and above, respectively, the absorption edge for elemental mapping. At the absorption edge the mass absorption coefficient of the edge element jumps from $\mu_M(E_1)$ to $\mu_M(E_2)$, whereas the coefficient of the matrix falls off proportional to E^{-3}.

2. Theory

2.1. Linear and mass absorption coefficient

In STXM, the absorption of X-rays is measured as they pass through the sample. The attenuation of the X-ray beam can be calculated from the following equation,

$$I(E) = I_0(E)\exp[-\mu(E)t], \tag{1}$$

where $I_0(E)$ is the incident light intensity, $I(E)$ is the transmitted light intensity, t is the sample thickness, and $\mu(E)$ is the linear absorption coefficient (Cullity, 1978). A convenient way to characterize the X-ray absorption is to define the optical density $D(E)$ of a thin film as

$$D(E) = -\ln\frac{I(E)}{I_0(E)} = \mu(E)\,t = \sum_{i=1}^{n}\mu_i(E)\,t_i, \tag{2}$$

where E denotes the photon energy and n is the number of elements contained in the sample. The Lambert–Beer Law (Beer, 1852) was used. Thus, the optical density ratio of the corresponding pixels in the two images can be calculated as the following,

$$\frac{D(E_2)}{D(E_1)} = \frac{\mu_l(E_2)\,t}{\mu_l(E_1)\,t} = \frac{\sum_{i=1}^{n}\mu_i(E_2)\,t_i}{\sum_{i=1}^{n}\mu_i(E_1)\,t_i}. \tag{3}$$

Another type of absorption coefficient, the mass absorption coefficient μ_M of an element, does not rely on the density of matter. Thus, the linear absorption coefficient μ_l can be described in terms of the density $\rho(z_i)$ and the mass absorption coefficient of each element as follows (Okuno *et al.*, 2006),

$$\begin{aligned}\mu_l &= \mu_M(z_1)\,\rho(z_1) + \mu_M(z_2)\,\rho(z_2) + \ldots + \mu_M(z_n)\,\rho(z_n)\\ &= \sum_i \mu_M(z_i)\,\rho(z_i),\end{aligned} \tag{4}$$

where z_i is the atomic number of the ith element in the sample.

The specific resonant absorption transition arises from excitation of an electron from a specific inner shell of the element. Fig. 1 illustrates the behaviours of the mass attenuation coefficients of the element under consideration (an edge element) and of the other specimen constituents, which are called the *matrix* in the following. The images are acquired at the energies E_1 (below the absorption edge) and E_2 (above the absorption edge), as noted in the figure, where the mass attenuation coefficients of the element z considered are $\mu_M(E_1, z)$ and $\mu_M(E_2, z)$, respectively. At E_1 and E_2, formula (4) can be written as the following,

$$\mu_M(E_1, z)\rho_z + \mu_l(E_1, \text{others}) = \mu_l(E_1), \tag{5}$$

$$\mu_M(E_2, z)\rho_z + \mu_l(E_2, \text{others}) = \mu_l(E_2), \tag{6}$$

where $\mu_l(E, \text{others})$ is the total linear absorption coefficient of all the other specimen constituents.

In Fig. 1, the absorption coefficient of the element z under consideration has a sudden jump, but, for all the other specimen constituents whose absorption edges are located away from the energy range considered, the absorption coefficients vary slowly and are proportional to E^{-3},

$$\mu = AE^{-3}, \tag{7}$$

where A is a constant (Engström, 1962). The main difference between the two images obtained at E_1 and E_2 is associated with the absorption jump of the element under consideration. All the other specimen constituents also contribute to the image difference, but their contribution is very small compared with that of the considered element. Thus, the difference between the two images can be used to map the element distribution.

The traditional subtraction method requires calculating the difference between their optical densities and histograms by subtracting the signal values of the image at E_1 from those at E_2 and then choosing a threshold value at 1σ of the background peak value, which is one standard deviation of the background noise distribution (De Stasio *et al.*, 2005). However, in our new method, we calculate the optical density

ratio of the corresponding pixels of the two images to obtain a ratio-contrast image, in which the pixel that has a ratio value bigger than a certain threshold is considered to contain the element of interest.

2.2. The threshold value

In the dual-energy absorption ratio-contrast image method, the threshold is a very important parameter that determines whether a pixel contains the element of interest. If we suppose a pixel does not contain the element of interest, then the density of that element, ρ_z, is equal to zero at that pixel and equations (5) and (6) have the following form,

$$\mu_1(E_1, \text{others}) = \mu_1(E_1), \tag{8}$$

$$\mu_1(E_2, \text{others}) = \mu_1(E_2). \tag{9}$$

We can calculate the theoretical threshold from equations (3), (8) and (9),

$$K_{\text{theory}} = \frac{\mu_1(E_2, \text{others})}{\mu_1(E_1, \text{others})}. \tag{10}$$

If one pixel contains the element of interest, or element z, then its contribution to the difference between the two images is much larger and the ratio of equations (5) and (6) should be greater than K_{theory}. Therefore, K_{theory} is the threshold value that determines whether a pixel contains the element of interest. If we know the reference spectra of all the constituents of a sample, the threshold can be calculated from (10). In many cases, particularly in biology or environmental science, the specimen cannot be assumed to be made up of a simple combination of a limited number of components for which reference spectra are known *a priori*. To determine the threshold of these complex samples, (10) can be simplified using the approximation (7),

$$K_{\text{theory}} = \frac{\mu_1(E_1, \text{others})}{\mu_1(E_2, \text{others})} = \frac{A/(E_1)^3}{A/(E_2)^3} = \left(\frac{E_2}{E_1}\right)^3. \tag{11}$$

Detector fluctuation and measurement error always exist and cause the real threshold to deviate from the theoretical one, $K_{\text{deviation}}$; this deviation must be considered during data analysis. In theory, the ratios of the optical density of the two images should be equal to or larger than the theoretical threshold value all the time. However, the practical ratio values may be below the theoretical threshold because of detector fluctuation or measurement error. We can calculate the standard deviation of the ratio values that are below the theoretical threshold value to determine $K_{\text{deviation}}$. In the subtraction method, K_{theory} is set to zero, while in the ratio method it could be approximately set to 1. However, we calculate K_{theory} according to formula (11) because the contribution of all the other sample constituents to the difference of the two images cannot be ignored; otherwise portions of the element distribution may be missing. Therefore, the real threshold value is the sum of K_{theory} and $K_{\text{deviation}}$,

$$K_{\text{real}} = K_{\text{theory}} + K_{\text{deviation}}. \tag{12}$$

2.3. The mass density

We can calculate a map of the mass density M of the considered element using formulas (5), (6) and (7) without knowing the composition of the matrix when we are judging whether or not a pixel contains the element of interest. We can obtain two equations using formulas (2) and (7),

$$\mu_{\text{M}}(E_1)\rho_z t_z + \frac{A t_{\text{others}}}{(E_1)^3} = D(E_1), \tag{13}$$

$$\mu_{\text{M}}(E_2)\rho_z t_z + \frac{A t_{\text{others}}}{(E_2)^3} = D(E_2), \tag{14}$$

where t_{others} is the total thickness of all the other sample constituents and the values of $\mu_{\text{M}}(E)$ can be found on the web (CXRO, 2009). Solving the equations provides the mass density M of the considered element in that pixel,

$$M = \rho_z t_z = \frac{D(E_2)(E_2/E_1)^3 - D(E_1)}{\mu_{\text{M}}(E_2)(E_2/E_1)^3 - \mu_{\text{M}}(E_1)}. \tag{15}$$

The expression (in terms of λ) was first obtained by Engström (Engström, 1962).

3. Experimental data analysis

We applied the new method to analyse the recent results measured by the BL08U STXM at the Shanghai Synchrotron Radiation Facility.

3.1. Example 1

The distribution of oxygen elements on a pre-oxidized polyacrylonitrile fibre cross section was researched by a group at the Institute of Chemistry Chinese Academy of Sciences. Fig. 2 shows the two absorption-contrast images of pre-oxidized polyacrylonitrile fibre cross sections at E_2 = 528.5 eV (Fig. 2*a*) and E_1 = 532.5 eV (Fig. 2*b*). The difference between the two images is not significant because the total quantity of oxygen elements in the sample is very small. Thus, the oxygen element distribution cannot be seen directly from the two images.

The threshold for dual-energy absorption-contrast analysis of the two images was calculated to be 1.157 for the ratio method and 0.038 for the subtraction method. Then, the distribution of oxygen with the threshold restriction was obtained using both methods and is shown in Fig. 3, where the bright white pixels contain oxygen. The results of the two methods are in accordance with each other and agree well with the predicted distribution trend that oxygen elements of the sample are mainly located at the surrounding borders of the pre-oxidized polyacrylonitrile fibre cross section. Because the results are in agreement, we can assume that the proposed method provides accurate results. The framed areas in Fig. 3 identify regions where the methods give different results.

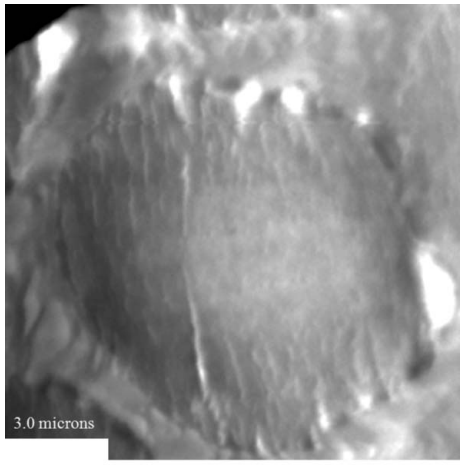

(*a*)

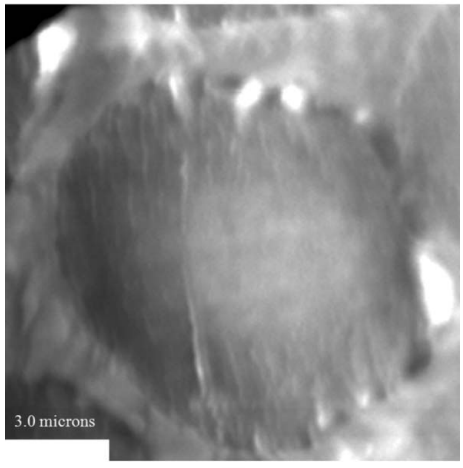

(*b*)

Figure 2
Two absorption-contrast images of pre-oxidized polyacrylonitrile fibre cross section at E_2 = 528.5 eV (*a*) and E_1 = 532.5 eV (*b*). The image size, step and number of pixels are 13 μm × 13 μm, 50 nm and 261 × 261, respectively. The difference between the two images is not evident to the naked eye.

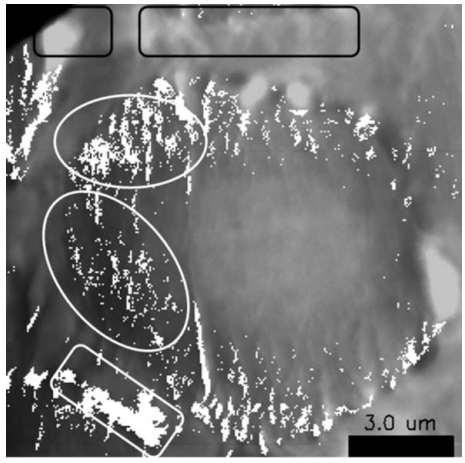

(*a*)

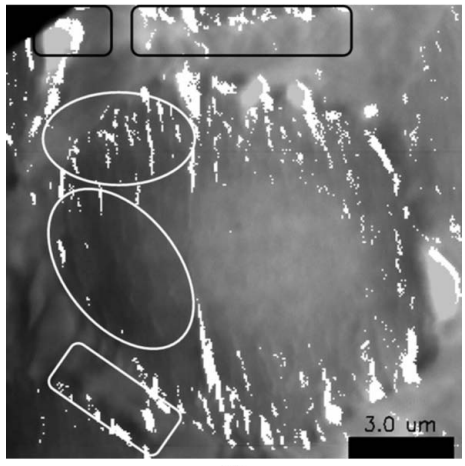

(*b*)

Figure 3
Oxygen element distribution maps based on the thresholds calculated by the two methods: (*a*) the new ratio method and (*b*) the traditional KES method. The bright white pixels contain oxygen. The scale of the two images is 13 μm × 13 μm or 261 × 261 pixels. The black and white frames indicate where significant differences exist between the two images: the fine dot distribution of oxygen is evident using the ratio method, but it is missing in results from the traditional subtraction method (white frames); the noise in the subtraction method is discarded by the ratio method (black frames).

From these areas it can be seen that the oxygen fine distribution is present in the results from the ratio method in the white framed areas, whereas it is missing in these areas in the results given by the subtraction method. In the meantime, the black framed areas show that the subtraction method yields some abnormal noise that is discarded by the ratio method. Therefore, these differences further indicate the effectiveness and advantages of the ratio analysis method compared with the traditional subtraction method.

The results shown in Fig. 2 are in good accordance with each other, which suggests that neither method is defective. We can clearly see that there is a finer element distribution in the areas with white frames in Fig. 3(*a*) compared with that in the corresponding area in Fig. 3(*b*). The fine distribution in image (*a*) does not appear in image (*b*), which indicates that some of the pixels are identified incorrectly in the traditional method because of the improper threshold value. The fine distribution of the considered element illustrates the advantages of the 30 nm high resolution of the SSRF STXM endstation and the ratio-contrast analysis method for mapping element distributions.

3.2. Example 2

Another experiment involved human cervical carcinoma samples that were provided by a research group from the Laboratory for Bio-Environmental Effects of Nanomaterials and Nanosafety and the Key Laboratory of Nuclear Analytical Techniques, Institute of High Energy Physics, Chinese Academy of Sciences. The sample was first treated by citrate acid modified by ferroferric oxide nanoparticles (10 nm) with a 200 p.p.m. concentration. Then, it was fixed and dropped directly onto a window of silicon nitride that was installed on the sample holder of the STXM device.

Two photon energies were chosen, E_1 = 703.1 eV and E_2 = 706.3 eV, which are just below and above, respectively, the

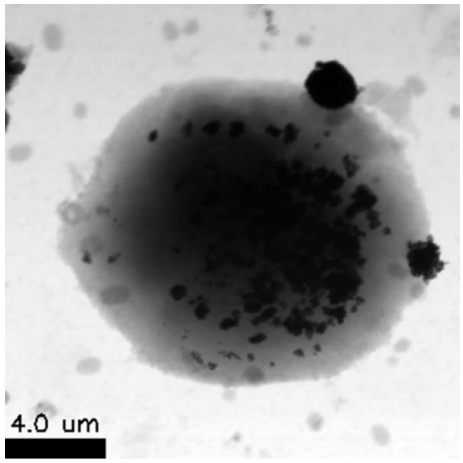

(*a*)

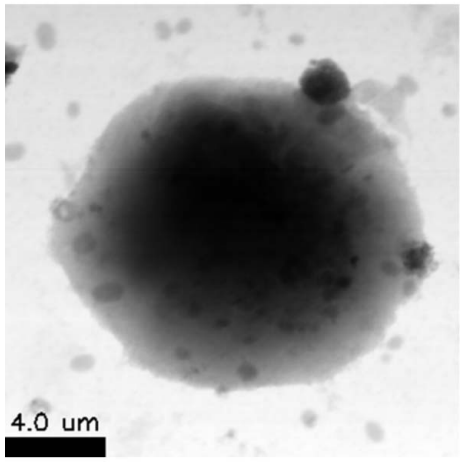

(*b*)

Figure 4
Two absorption-contrast images of a human cervical carcinoma cell at $E_2 = 706.3$ eV (*a*) and $E_1 = 703.1$ eV (*b*). The image size, step and number of pixels are 18 µm × 18 µm, 50 nm and 360 × 360, respectively. The image (*a*) obtained at $E_2 = 706.3$ eV has intense absorption, and the signal of image (*b*) obtained at $E_1 = 703.1$ eV is flat compared with image (*a*).

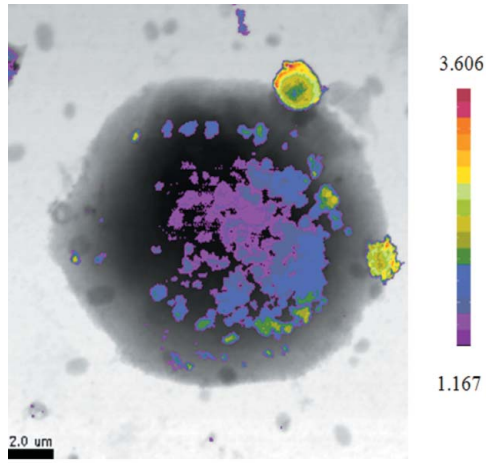

(*a*)

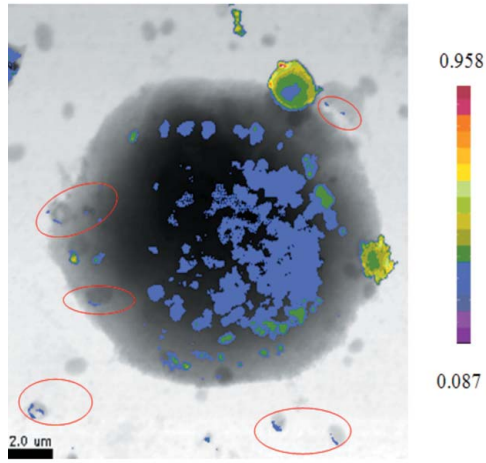

(*b*)

Figure 5
The ferroferric oxide distribution calculated using the subtraction and ratio methods. The image size, step and number of pixels are 17.7 µm × 18 µm, 50 nm and 354 × 360, respectively, after shifting and clipping. The red frame areas of the two images denote the ferroferric oxide distribution. The range of ratio contrast (colourful regions) noted by the colour bar in (*a*) is from 1.168 to 3.606, where 1.168 is the threshold and 3.6055 is the maximum contrast ratio, while the colour bar in (*b*) shows the subtraction contrast from 0.087 to 0.958, where 0.087 is the threshold and 0.958 is the maximum of subtraction contrast.

absorption edge of ferroferric oxide, to scan the sample pixel by pixel. Fig. 4 shows the absorption-contrast images of a human cervical carcinoma cell at two photon energies. Fig. 4(*a*) was obtained at $E_2 = 706.3$ eV and shows various intense absorption areas compared with Fig. 4(*b*), which was obtained at $E_1 = 703$ eV and shows relatively flat signals. We converted the absorption contrasts of the two images into optical densities and then used the two methods, *i.e.* ratio and subtraction analysis, to calculate the considered element distribution after the two images were registered. Using the ratio method, the experimental data for this cell sample were analysed, and the threshold value was calculated to be 1.168. Then, the ferroferric oxide distribution was acquired and shown with colourful pixels overlapped on the original image in Fig. 5(*a*). The subtraction method was used for the same experimental data; the threshold value was calculated as 0.087, and the corresponding result is shown in Fig. 5(*b*). The range of ratio contrast (colourful regions) noted by the colour bar in (*a*) is from 1.168 to 3.606, where 1.168 is the threshold and 3.606 is the maximum of contrast ratio, while the colour bar in (*b*) shows the subtraction contrast, which ranges from 0.087 to 0.958, where 0.087 is the threshold and 0.958 is the maximum subtraction contrast.

The colour area in Figs. 5(*a*) and 5(*b*) contain the element of interest. The results from the two methods are in accordance. Nevertheless, the signals outlined by the red elliptic areas in Fig. 5(*b*) are actually noise because there is no significant absorption change within these areas between the two energies; thus, they were discarded by the ratio method, as shown in Fig. 5(*a*). The pink area contained in Fig. 5(*a*) is removed in Fig. 5(*b*) which was calculated by the subtraction method but ignored the contribution of the absorption changes of other elements.

4. Conclusions

Using the dual-energy ratio-contrast image method, the two-dimensional spatial distribution of an element of interest in the sample can be mapped and calculated quantitatively from its absorption difference at two photon energies, E_1 and E_2, which are just below and above, respectively, the absorption edge of the chosen element. The new method has evident advantages compared with the traditional subtraction method. The analysis results show that it can accurately map the element distribution and is sensitive to the element of interest while reducing the noise. In the new method the definition and theoretical calculation of the threshold are simpler and its physical meaning is clearer. With the ratio method we can determine the information missing from the element distribution, as in the traditional subtraction method, and overcome the unfavourable influence of the absorption differences that result from the other sample constituents. Therefore, the dual-energy ratio-contrast image method provides new, simple and fast data analysis to map an element of interest with X-ray spectromicroscopy.

References

Beer, A. (1852). *Ann. Phys.* **86**, 78–88.

Bewer, B., Zhang, H., Zhu, Y., Zhang, L., George, G. N., Pickering, I. J. & Chapman, D. (2008). *Rev. Sci. Instrum.* **79**, 085102.

Cullity, B. D. (1978). *Elements of X-ray Diffraction*, 2nd ed. New Jersey: Addison-Wesley.

CXRO (2009). *X-ray Interactions With Matter*, http://www-cxro.lbl.gov/optical_constants/.

De Stasio, G. *et al.* (2005). *Neurochem. Res.*, **27**, 387–398.

Elleaume, H. *et al.* (2000). *Cell. Mol. Biol.* **46**, 1065–1075.

Engström, A. (1962). *X-ray Microanalysis in Biology and Medicine.* New York: Elsevier.

Frazer, B. H., Sonderegger, B. R., Gilbert, B., Richter, K. L., Salt, C., Wiese, L. M., Rajesh, D., Howard, S. P., Fowler, J. F., Mehta, M. P. & De Stasio, G. (2003). *7th International Conference on X-ray Microscopy*, Grenoble, France, 28 July–2 August 2002, pp. 349–352.

Fukagawa, H., Noda, C., Suzuki, Y., Hasegawa, S., Ando, M., Hyodo, K., Nishimura, K., Akisada, M., Takenaka, E., Hosaka, R. & Toyofuku, F. (1989). *Rev. Sci. Instrum.* **60**, 2268–2271.

Houk, T. L., Kruger, R. A., Mistretta, C. A., Riederer, S. J., Shaw, C. G., Lancaster, J. C. & Flemming, D. C. (1979). *Invest. Radiol.* **14**, 270–278.

Jacobson, B. (1953). *Acta Radiol.* **39**, 437–452.

Kruger, R. A., Mistretta, C. A., Crummy, A. B., Sackett, J. F., Goodsitt, M. M., Riederer, S. J., Houk, T. L., Shaw, C. G. & Fleming, D. (1977). *Radiology*, **125**, 243–245.

Krug, K., Dik, J. & Leeum, M. (2006). *Appl. Phys. A*, **83**, 247–251.

Lerotic, M., Jacobsen, C., Schäfer, T. & Vogt, S. (2004). *Ultramicroscopy*, **100**, 35–37.

Lewis, R. (1997). *Phys. Med. Biol.* **42**, 1213–1243.

Okuno, K., Ohigashi, T., Kamiyama, S., Hirai, S., Matsubara, J., Watanabe, N. & Aoki, S. (2006). Editors. *Proceedings of the 8th International Conference on X-ray Microscopy*, Himeji, Japan, 26–30 July 2006, pp. 357–358.

Rarback, H., Cinotti, F., Jacobsen, C., Kenney, J. M., Kirz, J. & Rosser, R. (1987). *Biol. Trace Elem. Res.* **13**, 103–113.

Sarnelli, A., Elleaume, H., Taibi, A., Gambaccini, M. & Bravin, A. (2006). *Phys. Med. Biol.* **51**, 4311–4328.

Sarnelli, A., Taibi, A., Tuffanelli, A., Baldazzi, G., Bollini, D., Cabal Rodriguez, A. E., Gombia, M., Prino, F., Ramello, L., Tomassi, E. & Gambaccini, M. (2004). *Phys. Med. Biol.* **49**, 3291–3305.

Suortti, P. & Thomlinson, W. (2003). *Phys. Med. Biol.* **7**, 1–35.

Takeda, T., Itai, Y., Hyodo, K., Ando, M., Akatsuka, T. & Uyama, C. (1998). *J. Synchrotron Rad.* **5**, 326–332.

Umetani, K., Ueki, H., Ueda, K., Hirai, T., Takeda, T., Doi, T., Wu, J., Itai, Y. & Akisada, M. (1996). *J. Synchrotron Rad.* **3**, 136–144.